PAPER

Check for updates

Facile synthesis of silver/gold alloy nanoparticles for ultra-sensitive rhodamine B detection

Thi Thu Ha Pham,[a] Nguyen Dac Dien[b] and Xuan Hoa Vu ⓘD *[cd]

The synthesis of Ag/Au nanoparticles (NPs) in a controlled manner has been a challenge for a long time. The aim of this report is to present a systematic study on the fabrication, characterization of Ag/Au alloy NP-based surface-enhanced Raman spectroscopy (SERS) substrates. Silver (Ag) and gold (Au) colloidal NPs were prepared by chemical reduction route of the corresponding metal salts by trisodium citrate (TSC). Ag/Au alloy nanoparticles with varying molar fractions are prepared in aqueous solution by the simultaneous reduction of $AgNO_3$ and $HAuCl_4$ by TSC. The composition of Ag and Au in the alloy samples was controlled by tuning the molar ratio of Ag^+/Au^{3+} in the mixture solution. The morphologies of the different products were characterized by TEM, and the size of obtained samples was in the range of 40 to 60 nm. The resulting samples were denoted as AgNPs, AuNPs, Ag_3Au, AgAu, and $AgAu_3$ NPs. In order to compare the optical property of the Ag/Au alloy and Ag/Au mixture, we mixed the pure Ag and Au NPs with different ratios to obtain the aggregated nanoparticles. Ag/Au alloy NPs were demonstrated as an ultrasensitive SERS substrate for the detection of rhodamine B (RhB) molecules. The concentration of RhB ranged from 10^{-11} to 10^{-5} M. The effect of the Au content on the optical and SERS properties of the Ag/Au alloys was studied. The obtained results show that the Au content in the Ag/Au alloys play an important role in the physical properties of Ag/Au alloy NPs. The SERS spectra of RhB from the as-prepared Ag/Au alloy NP substrates indicated the superior enhancement with high reproducibility and sensitivity compared to those of Ag or Au samples. Interestingly, the highest SERS activity was achieved for the Ag_3Au sample with an enhancement factor larger than 10^{10} for 10^{-11} M RhB and a limit of detection (LOD) at 10^{-11} M, as well as good long-term stability after storage for 1 year. As far as we know, this is the highest sensitivity record of RhB by SERS detection. Furthermore, the composition-dependent SERS activity was explained in detail. These advantages demonstrated the potential for growing Ag/Au alloy NP-based SERS substrates in food safety and bioanalysis.

1. Introduction

Recently, Ag/Au bimetallic nanostructures have attracted great attention in nanoscience research, as well as the impressive developments in mobile device technologies, owing to their unique optical, electronic and catalytic properties.[1–3] For two atomic-type containing materials, gold and silver are the most popular elements used in recent studies.[4] The noble metals (Ag, Au) have a broad absorption band in the visible region of the electromagnetic spectrum.[5] Gold (Au) shows inertia, stability and has low catalytic activity compared to silver. The synergistic effect of Au and Ag enhanced the catalytic performance of the Ag/Au alloy compared with the Ag nanoparticles (NPs), and the effect on the optical properties of the Ag/Au alloy. The structural and catalytic changes have been examined for the admixture of gold to silver.[6,7] This property was used in many areas, including antibacterial,[8] bioimaging,[9] bio-labeling,[10] catalysis,[11,12] drug delivery, cancer therapy,[13] nanophotonics,[14] optoelectronics,[15] molecular detection,[16,17] and nanoscale optical biosensors.[18] The physical and chemical properties of nanomaterials are determined by their dimensions and shapes. In the nanometer regime, as the percentage of surface atoms starts taking over bulk atoms, their atomic coordination at the surface decreases, and their catalytic property increases.[19] For instance, metal nanoparticles are very important as catalysts, and especially attractive for biomedical and nanomedicine applications because of their high surface-to-volume ratio.[3] Therefore, controlling their size and morphology has garnered significant research interest.[20,21] However, the synthesis of Ag/Au alloy NPs with precise composition and high surface is still a great challenge.[22] Numerous strategies have been implemented to fabricate Ag/Au alloy nanostructures with desired optical and surface

[a]Faculty of Chemistry, TNU-University of Sciences, Tan Thinh Ward, Thai Nguyen City, Vietnam

[b]Faculty of Labour Protection, Vietnam Trade Union University, 169 Tay Son, Dong Da District, Hanoi City, Vietnam

[c]Faculty of Physics and Technology, TNU-University of Sciences, Tan Thinh Ward, Thai Nguyen City, Vietnam. E-mail: hoavx@tnus.edu.vn

[d]Institute of Science and Technoloy, TNU-University of Sciences, Tan Thinh Ward, Thai Nguyen City, Vietnam

properties, including capillary micro-reaction,[22] laser ablation in liquids,[2] citrate reduction of Ag and Au salts,[3] photosynthetic route,[8,23] and galvanic replacement reaction.[24]

Raman spectroscopy is sensitive to the vibrational frequencies of molecules, and therefore obtains unique molecule fingerprints, which is the high specificity of Raman spectroscopy.[25] However, Raman scattering is inherently weak and it is difficult to detect substances in small concentrations. Surface-enhanced Raman scattering (SERS) is a powerful, sensitive, rapid, noninvasive and nondestructive spectroscopy technique, which could provide molecular-level information of analytes adsorbed on the active substrates.[26] The enormous enhancement of the Raman signal of the target molecules located at the vicinity of the SERS-active metal nanostructures allows SERS to be employed for the detection of substrates at extremely low concentrations.[27] SERS was first observed in 1974,[28] and the single molecule sensitivity of SERS was initially shown by Nie in 1997.[29] To date, SERS overcomes the shortcoming of the low sensitivity of conventional Raman spectroscopy, and many applications of SERS spectra have achieved fruitful results.[30] The interaction of the incident EM field with metal NPs induces a collective and coherent electron oscillation in the vicinity of the NPs, which is called plasmons. The huge enhancement of Raman signals in SERS results from the collective oscillations of the conduction electrons in the surface of plasmonic nanostructures, called the localized surface plasmon resonance (LSPR). The optical excitation of the LSPR of silver and gold NPs results in strong enhancement of the local electromagnetic (EM) field near the NP surface, which is the dominant contributor to the SERS sensing mechanism.[18] The LSPR can be modulated from the ultraviolet (UV) region to the infra-red (IR) region of the electromagnetic (EM) spectrum, depending on the size and shape of the metallic NPs.[1] The Raman signal of the adsorbed molecules is augmented by a strong EM field at the interface and surface of the plasmonic nanoparticles. The overlap region between the adjacent NPs is called "hotspots", where the local field enhancement is superior. An ideal SERS substrate should have a large number of hotspots, capability of low-detection limit, uniformity, reproducibility and stability. The chemical enhancement of the SERS intensity because of the charge transfer (CT) mechanism between the substrate and the analyte is generally 1–3 orders of magnitude smaller than that of the EM mechanism.[2] Despite the equivocal selection rule and limited application to a few metals, the SERS technique can monitor the adsorbates on metallic substrates at the sub-monolayer coverage limit.[31] SERS promises numerous applications in chemical and biological sensing, environmental monitoring and food safety (such as the detection of drugs,[13] explosives,[2] bacteria,[7] influenza virus,[32] rhodamine 6G (R6G),[26,30] rhodamine B (RhB),[33,34] malachite green (MG),[26] thiram,[35,36] melamine,[37] thiophenol (TP)[38]) due to its single molecule sensitivity and selectivity.[39,40] The sensitivity of SERS detection is determined by noble metal nanoparticles.[41] Ag and Au are extensively utilized materials in the preparation of SERS substrates due to their LSPR in the visible region.[2] The surface plasmon efficiency of Ag is greater than that for Au.[27] However, the susceptibility of AgNPs to oxidation leads to the change of

their morphology, which results in the deterioration of their SERS stability.[42] Additionally, the synthesized AgNPs were not homogeneous in size and shape, leading to poor reproducibility in SERS measurement. In contrast, AuNPs were more stable, but less sensitive than AgNPs.[43] Combining Ag and Au helps in tuning the surface plasmon resonance (SPR) of the Ag/Au nanostructures to any wavelength in the visible region of the spectrum. Recently, bimetallic silver/gold NPs have drawn remarkable interests as SERS substrates. Rongchao Mei *et al.* prepared bimetallic gold core–silver shell SERS tags for multiplex detection, containing 4-nitrothiophenol, 4-aminothiophenol, 1,4-benzenedithiol, and 4-fluorothiophenol.[35] Jian-Jun Li and co-workers coated silver on gold nanostars to produce a super-multibranched Au–Ag nanostructure, which has been used to detect thiram.[36] Dapeng Xu and his colleagues fabricated gold nanoparticles/silver nanowires composites to detect rhodamine B (RhB).[34] Hui Wang and his group synthesized core–shell Au@Ag nanoparticles to determine RhB in food products.[33] Generally, it is desirable to prepare uniform and size-controlled Ag/Au alloy NPs, which combine the superior properties of classic gold and silver NPs, *i.e.*, inherit the ideal signal enhancement ability of Ag nanostructures and the stability of Au nanostructures. The obtained alloy NPs could be applied as SERS substrates for the trace detection of various samples with high reproducibility and effect in the SERS performance.[44] This alloy structure gained the strong and specific Raman signal of analytes adsorbed on the surface, making them a powerful candidate for reliable quantitative analysis. The SERS applications in real samples promoted the value of Ag/Au nanoparticles.[45] To the best of our knowledge, the RhB sensing based on a novel SERS-active nanosubstrate using Ag/Au alloy NPs has not been reported up to now.

In this paper, the co-reduction of Ag$^+$ and Au^{3+} salts in aqueous solution was adopted to synthesize Ag/Au alloy NPs, where sodium citrate was taken as a reductant and polyvinyl pyrrolidone (PVP) as a surfactant. We report here an improved preparation method of the Ag/Au alloy NPs with the size in the range of 40–60 nm. The morphological uniformity and size distribution of the products were excellent. Interestingly, different Ag/Au alloy NPs samples can be developed by simply changing the silver and gold precursor ratio, which illustrated the generality and versatility of the synthesis procedure. The morphology of the alloy NPs was examined using transmission electron microscopy (TEM). The lattice constants of samples and the formation of homogeneous Ag/Au alloy nanocrystals were confirmed by high-resolution transmission electron microscopy (HRTEM) technique. The optical property (plasmon absorption) was analyzed by ultraviolet-visible (UV-Vis) spectroscopy. The chemical structure was determined through Fourier transform infrared (FTIR) spectra. The element component of the materials was evaluated using energy dispersive X-ray spectroscopy (EDS). The silver and gold atomic distribution was characterized by energy dispersive X-ray (EDX) elemental mapping. The crystal structure and size were recorded by the X-ray diffraction (XRD) pattern. The SERS spectra of rhodamine B excited by an efficient green laser (532 nm) using the as-prepared Ag/Au alloy NPs as the SERS-active substrate

indicated that the optimal composition of Ag : Au was 3 : 1. Importantly, the enhancement factor (EF) of the Ag$_3$Au alloy NPs approaches more than 10^{10} for rhodamine B molecules at a concentration of 10^{-11} M. Here, the SERS method based on the Ag/Au alloy NPs is convenient, rapid, sensitive and provides fingerprint identification for RhB. The experimental results revealed that the lowest RhB detection concentration was 10^{-11} M, and can also be well maintained after storage for 1 year. The improved sensitivity demonstrated the potential application of the as-prepared Ag/Au alloy NPs in food safety for detecting RhB in aqueous solution. Our work demonstrated the ability to identify and semi-quantify trace amounts of RhB, and we provide herein a detailed discussion about the performance, fabrication and physical characterization of our SERS active nanomaterials.
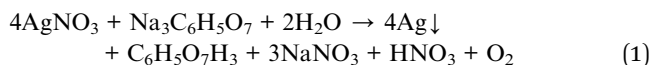
2. Experimental

2.1. Materials

Silver nitrate (AgNO$_3$, 99.92% pure), chloroauric acid (HAuCl$_4$·3H$_2$O, 99.99%), trisodium citrate (TSC, Na$_3$C$_6$H$_5$O$_7$·2H$_2$O, 99%), rhodamine B (RhB, C$_{28}$H$_{31}$ClN$_2$O$_3$), and polyvinyl pyrrolidone (PVP, molar weight (MW) 29 000 g mol^{-1}) were all purchased from Merck (Germany). All of the above chemicals were of reagent grade and used as received without further treatment. Doubly distilled water was used in all aqueous solutions and rinsing procedures to clean all glassware prior to use. The pH of the reaction solution was measured with a digital pH/ion meter.
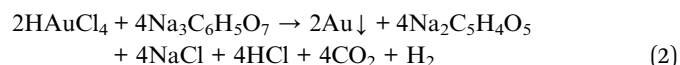
2.2. Synthesis of Ag, Au, Ag/Au alloy nanoparticles

Silver nanoparticles (AgNPs) were prepared *via* reduction method, where silver nitrate (AgNO$_3$) was reduced by trisodium citrate (TSC, C$_6$H$_5$O$_7$H$_3$). In a typical process, fifty microliters of AgNO$_3$ (0.02 M) was added to forty milliliters of water in a flask and heated to boiling, then one hundred microliters of 2% TSC was slowly added to the above solution drop by drop using a syringe with the temperature kept at 100 °C at the meantime. The mixture was vigorously stirred for 1 h to complete the reduction of the Ag$^+$ ions to Ag atoms. The solution color gradually turned to a faint yellow color, and finally changed into a brilliant yellow color after 1 h, revealing the formation of AgNPs. After cooling naturally to room temperature, the obtained product was the AgNPs colloid. Finally, the as-prepared AgNPs sediments were washed by deionized (DI) water three times, and then dried in a desiccator overnight. The reaction of the reduction of Ag$^+$ can be expressed as follows:

$$4AgNO_3 + Na_3C_6H_5O_7 + 2H_2O \rightarrow 4Ag\downarrow \\ + C_6H_5O_7H_3 + 3NaNO_3 + HNO_3 + O_2 \qquad (1)$$

Following this way, the colloidal dispersions of gold nanoparticles (AuNPs) were prepared by the aqueous reduction method of tetrachloroauric acid (HAuCl$_4$) using TSC, which was proposed in 1973 by G. Frens.[46] In a typical experiment of fabricating AuNPs, a volume of 50 μl of aqueous 20 mM chloroauric acid (HAuCl$_4$) solution was added to 40 ml distilled water and heated to boiling, then 100 μl of 2% TSC was added to the HAuCl$_4$ solution under vigorous stirring and boiling was continued for *ca.* 1 h. A condenser was utilized to prevent the evaporation of the solvent. The instantaneous appearance of a light red color signaled the formation of AuNPs. The color of the colloid changed to wine red on increasing the reaction time to 1 h. The pH value of the reaction solution was measured to be 7.2, and was not changed to maintain the colloidal stability. Then, the reaction solution was left to cool to room temperature. The Au^{3+} ions were reduced to Au atoms as follows:

$$2HAuCl_4 + 4Na_3C_6H_5O_7 \rightarrow 2Au\downarrow + 4Na_2C_5H_4O_5 \\ + 4NaCl + 4HCl + 4CO_2 + H_2 \qquad (2)$$

The reaction that was previously applied in the preparation of the Ag/Au bimetallic nanostructures was modified to synthesize the Ag/Au alloy NPs.[47] Ag/Au alloy nanoparticles were synthesized by the reduction of changeable molar fractions of HAuCl$_4$·3H$_2$O and AgNO$_3$ using TSC as the reducing chemical and PVP as a stabilizing agent in water for the stabilization of the Ag/Au NPs. The composition of the Ag/Au alloy can be tuned by varying the molar ratio of Ag$^+$: Au^{3+} in the raw material (1 : 3, 1 : 1, and 3 : 1). Gold and silver ions are reduced simultaneously by sodium citrate in the same solution to form gold–silver alloy particles. The reaction involved numerous sequential processes: oxidative dissolution of the Ag atoms, reduction of the AuCl$_4^-$ ions and deposition of the Au atoms.[9] Metal NPs were produced by the growth of particles obtained from metal atoms, which are from ionic precursors. Since two metal precursors are involved in the reduction reactions, the co-reduction of Au and Ag salts is the simple method of preparing the Ag/Au alloy NPs. Briefly, 50 μl of 0.02 M aqueous HAuCl$_4$, 50 μl of 0.02 M aqueous AgNO$_3$ and 0.4 ml of PVP aqueous solution (0.0067 M) were added to 80 ml of deionized water at pH 7, and the solution was mixed by stirring. After about 5 min, 200 μl of 2% TSC was gradually added to the aforementioned mixture with stirring. The formation of bimetallic NPs is indicated by the color change of the 1 : 1 (Au : Ag) molar mixture from colorless to a light yellow color. The reaction mixture was vigorously stirred at 100 °C for 1 h, and then left to cool to room temperature naturally. The obtained NPs were the AgAu alloy. The procedure was repeated for varying Ag : Au molar ratios of 3 : 1 and 1 : 3 to obtain Ag$_3$Au and AgAu$_3$ NPs colloids, respectively, and the color varied from golden yellow to purple.

The schematic diagram of the fabrication process of the Ag/Au alloy NPs using solution reaction technology is shown in Fig. 1. First, aqueous solutions of the starting agents (AgNO$_3$ and HAuCl$_4$ salts) were mixed in the desired molar ratios by stirring for 5 min. Second, TSC and PVP were added to the reaction mixture with stirring. Finally, after stirred at 100 °C for 1 h, the Ag/Au alloy nanoparticles with different Ag/Au proportions were formed. The Ostwald ripening mechanism is characterized by the growth of large particles that receive the atoms from the smaller particles. The smaller particles are depleted by growth, shrink and eventually disappear.[48]
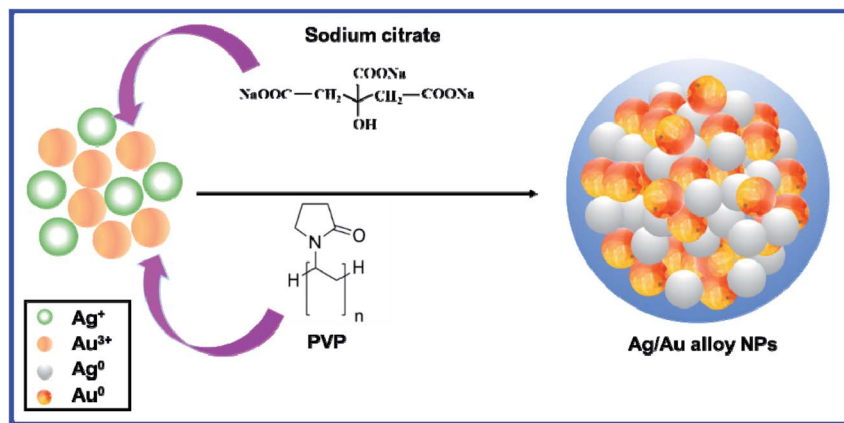
Fig. 1 Schematic illustration of the formation of the Ag/Au alloy NPs.

2.3. Characterization

The average particle size distribution of the Ag/Au alloy and their relative standard deviation were obtained by particle size analyzer (PSA, Delta Nano C, Beckman) using the dynamic light scattering (DLS) technique. EDS was applied to determine the detailed information on the elemental composition using a scanning electron microscope (SEM, Hitachi S4800, Japan) coupled with energy dispersive X-ray spectroscopy (EDS) detector, operated at an accelerating voltage of 18 kV. Optical absorption spectra of the as-synthesized colloids were recorded using a Jasco V-770 UV-Vis spectrophotometer in the wavelength range of 300–800 nm operated at a resolution of 1 nm to check the surface plasmon band, and to investigate the relationship between the composition of the Ag–Au and absorption wavelength. Their absorption studies were achieved by placing 3 ml of colloidal solution in 1 cm quartz cuvette of the UV-Vis spectrometer. A transmission electron microscope (TEM, JEOL JEM-1010) operated at an electron-accelerating voltage of 80 kV was used to observe the morphology and directly measure the size of nanoparticles. The sample for TEM and EDS was prepared by drop-casting the homogeneously dispersed Ag/Au alloy NPs solutions onto carbon-coated copper grids, and then left to evaporate overnight in air at room temperature. The HRTEM study was carried out with a JEOL JEM-1010 operating at 200 kV. Structural analyses of the as-synthesized nanoparticles were accomplished through XRD and FTIR spectra. XRD was recorded between the scan angles of 30° and 80° on a Bruker D8 Advance diffractometer (Germany) using the Cu-K$_\alpha$ line of $\lambda = 1.5406$ Å. A JASCO 4600 (Japan) spectrophotometer was employed to record the FTIR spectra to identify the functional groups present in the silver nanoparticles.

2.4. SERS measurement

In a typical SERS procedure, the nanoparticles sol was first centrifuged at 6000 rpm for 10 min in an ultracentrifuge several times to concentrate the colloids, and remove the excess reactants and supernatant. Smooth silicon wafers were cleaned using an acetone solution before use. Subsequently, the nanomaterial-based substrates were prepared by mixing 10 μl of

AgNPs, AuNPs, and Ag/Au alloy NPs sol with an equal volume of probe molecules (RhB) at the desired concentration (10^{-11} to 10^{-5} M). Then the resulting mixture was deposited onto a silicon wafer using a micropipette and allowed to dry completely in a desiccator for about 30 min before SERS measurements. All of the Raman spectra were acquired on a Xplora Raman microscope (Horiba, France) in the spectral range of 500–1800 cm^{-1}. A solid-state laser with the wavelength of 532 nm was used as the excitation source for SERS analysis. The 532 nm excitation line can support the resonant Raman of RhB, which drastically improved the SERS signals. The excitation light is focused on a circular point with diameter of about 3.8 μm by using a 100× microscopy objective lens. The exciting laser power on the sample was 3.2 mW, and the exposure time used for each spectrum was 8 s. To ensure the SERS activity was reliable, each spectrum was averaged by the Raman spectra from 8 different collecting points. The linear relationship between the Raman intensity (I_{SERS}) and the concentration of RhB was calculated to evaluate the calibration capability of the samples.

3. Results and discussion

3.1. UV-Vis absorption spectra

The color of the Ag/Au NPs colloid reflected its composition and micro-structure.[22] Solutions of these metal NPs show the fingerprint color, which is absent for the bulk material and their atomic mode. This property is attributed to the collective oscillation of the free conduction electrons induced by the alternating electromagnetic field of the incident light, which is called surface plasmons in the Mie theory.[49] The color changes in the reaction mixtures and formations of the characteristic absorption peaks were used to indicate the synthesis of Ag, Au, and Ag/Au alloy NPs through the reduction of Ag$^+$, Au^{3+} by TSC. The color of the Ag colloid is yellow, together with the significant characteristic SPR absorption peak at 396 nm (Fig. 2a). The color of the Au colloid is purple, which corresponds to its characteristic absorption peak at 530 nm, owing to the SPR of AuNPs. The color of the Ag/Au colloids gradually changed from yellow to purple with a shift in the characteristic absorption
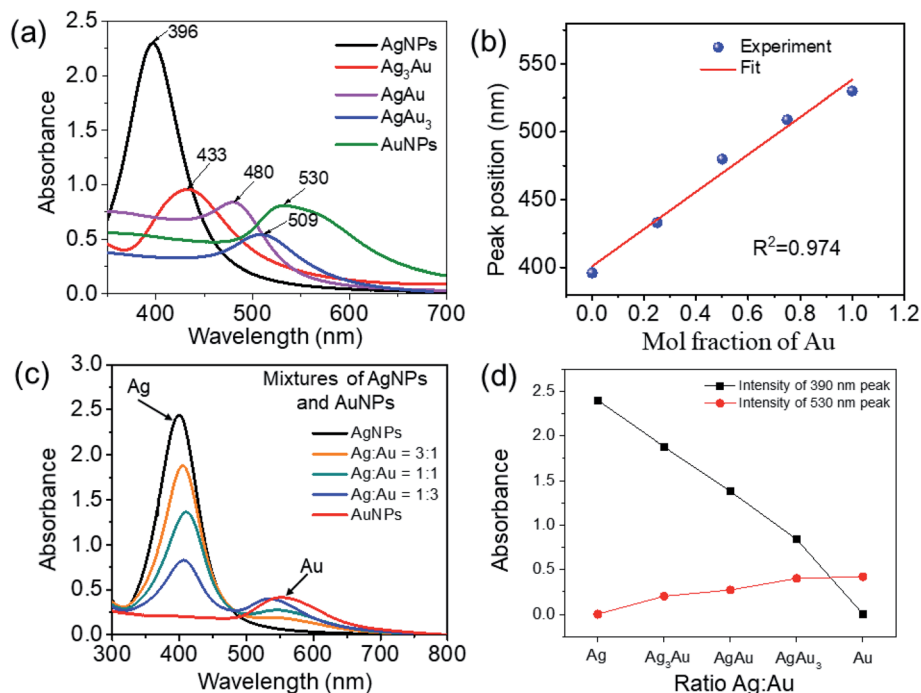
Fig. 2 (a) UV-Vis absorption spectra of pure gold, pure silver and silver−gold alloy nanoparticles with varying gold molar fractions. (b) The solid line is a linear fit of the absorption maximum to the gold molar fraction, where the spheres correspond to the experimental data. (c) UV-Vis spectra of mixtures of AgNPs and AuNPs with different ratios. (d) The curve of the absorbance intensity of the 390 nm and 530 nm peaks *versus* the Ag : Au ratio.

peak (433 nm to Ag₃Au, 480 nm to AgAu, and 509 nm to AgAu₃), indicating that the Ag/Au alloy NPs were formed.[22,23] The LSPR wavelength of the Ag/Au alloy NPs red-shifted about 113 nm, owing to the strong coupling effect between the Ag and Au atoms.

The optical property of the sample sols was characterized using UV-Vis absorption spectroscopy, and the extinction spectra for the Ag, Au, Ag/Au NPs in aqueous solutions are shown in Fig. 2a. UV-Vis spectroscopy of metallic NPs is highly sensitive to morphological variation. Metallic NPs exhibit characteristic absorption in the visible region due to the excitations from surface plasmon vibrations.[8] All samples display only a single plasmon absorption band in the UV-Vis region, which is characteristic of alloy NPs, indicating the homogeneity within the volume of the particles.[3] The optical absorptions vary between the $\lambda_{\max}$ values (*ca.* 396 nm for pure AgNPs and *ca.* 530 nm for pure AuNPs) of the monometallic colloids, which is in good agreement with a previous report.[50] AgNPs display stronger actual absorbance with higher plasmon energy than those of AuNPs, as reported in the literature.[8] An absorption band shoulder of AuNPs is located at about 560 nm. The maximum absorption band red-shift from 396 nm to 530 nm with an increasing amount of gold was due to plasmonic coupling between Ag and Au. The observation of this red shift in $\lambda_{\max}$ is typical of Ag/Au alloys,[8] which is attributed to the interaction between Au and Ag in the Ag/Au alloy NPs, providing a bimetallic synergistic effect for enhancing the SERS performance.[51] The alloy formation is presumed to be due to the simultaneous reduction of Ag and Au ions by TSC. When the

gold content in the alloy increases, the main dipolar resonance band red shifts and broadens. This single band is accompanied by a shoulder at 560 nm, corresponding to a quadrupolar resonance for AuNPs. The experimental absorbance data can be compared to calculation based on the standard Mie theory of spherical particles, which theoretically explains the size dependence of the surface plasmon absorption band.[48] Gold–silver alloy nanoparticles display the surface plasmon resonance (SPR) over a broad range of the UV-Vis spectrum due to the combined effect of the alloy composition and particle size. The wavelength of the SPR band depends on the size of the Ag/Au alloy nanoparticles as a second order polynomial with composition-dependent coefficients:

$$\lambda_{\max} = \alpha(x)D^2 + \beta(x)D + \gamma(x) \tag{3}$$

The SPR wavelength can be described by a third order function of the composition with size dependent coefficients:

$$\lambda_{\max} = \alpha'(D)x^3 + \beta'(D)x^2 + \gamma'(D)x + \delta'(D) \tag{4}$$

where x is the gold fraction and D is the particle diameter (nm). Mainly, the alloy composition determines the SPR wavelength, and the particle size is of secondary importance.[50]

The plot of the plasmon maximum $\lambda_{\max}$ against the Au molar fraction with the correlation coefficient ($R^2 = 0.989$) exhibited a quasi-linear relationship (Fig. 2b). The absorption peak is mainly attributed to the collective oscillation of the free conduction electrons induced by an interacting EM field.[27]

Nanoparticles with a size smaller than the wavelength of visible light powerfully absorb light because of surface plasmon resonance (SPR).[9] The UV-Vis kinetics for the formation of NPs showed that the characteristic absorbance decreased with the Au content, which was ascribed to the aggregation effect between silver and gold. The shift in the plasmon peak position from shorter to longer wavelengths, broadening of the SPR peak, and the change in the color of the colloidal solution all appear simultaneously. Moreover, the synthesized Ag, Au, Ag/Au alloy NPs exhibited no changes in color or SPR peak at room temperature within 6 months, indicating the stability of these samples. Fig. 2c shows the UV-Vis spectra of the physical mixture of Ag and Au NPs. Gold–silver composite colloids consisting of a mixture of gold and silver domains exhibited double plasmon absorption bands (390 and 550 nm) originating from the individual gold and silver domains. According to Anxin Jiao *et al.*, the LSPR of the Au/Ag nanocomposites is generally located at the red and near-infrared (NIR) region (>500 nm).[52]Fig. 2d shows the curve of the adsorbance intensity of the 390 nm and 530 nm peaks *versus* the Ag : Au ratio in the AgNPs : AuNPs mixtures. It can be seen that the intensity of the 390 nm peak decreases as the amount of AuNPs in the mixture increases, and completely vanishes for the pure AuNPs sample. In contrast, there was no adsorption peak at 530 nm for the pure AgNPs sample; this peak appears for the mixture samples and its intensity increases as the amount of AuNPs in the mixture increases. Generally, the 530 nm peak is much weaker than the 390 nm peak, which indicates that the optical property of silver is prominent compared to that of gold.

3.2. Electron microscopy and elemental analysis

The typical TEM image of AgNPs synthesized by reduction method is presented in Fig. 3a. Numerous spherical particles with a diameter of 6–8 nm are nearly monodispersed. The statistical analysis and the corresponding size distribution histogram are given in the inset of Fig. 3a. The DLS diameter is somewhat different from the TEM measurement because the DLS technique measures the hydrodynamic radius of the particles. The morphologies of the obtained Ag/Au nanoproducts are carefully investigated by TEM images with different magnifications in Fig. 3b–d. It can be seen that there are abundant well-dispersed Ag/Au NPs with uniform morphology and narrow size distribution in the range from 40 to 60 nm, which is drastically different from the size of the as-prepared well-dispersed AgNPs. Meanwhile, some NPs are agglomerated, which might be ascribed to the self-assembly of the PVP-adsorbed Ag/Au alloy NPs (Fig. 3c). In our experiment, the size was tuned by changing the molar ratio of $Ag^+ : Au^{3+}$. The average sizes of the Ag/Au alloy NPs with the Ag : Au molar ratio of 3 : 1, 1 : 1, and 1 : 3 are about 40 nm, 50 nm, and 60 nm, respectively.

The small variation in size demonstrated the homogeneous size distribution of the nanoparticles produced by the reduction with sodium citrate. Apparently, the shape of NPs was very uniform, and the size distribution of the NPs was homogeneous with almost quasi-spherical shaped particles. The isotropic nature of the particles may possibly be due to the efficient capping by PVP molecules, preventing any chance of agglomeration of the particles. The obtained Ag/Au alloy NPs depicted the high density of the NPs, leading to plenty of EM hotspots and will act as an efficient SERS substrate. The enlarged TEM images in the insets of Fig. 3b–d reveal a closer view of the Ag/Au alloy NPs. Fig. 3e is the TEM image of the sphere-like AuNPs with the size ranging from 30 nm to 60 nm.

Moreover, the high-resolution transmission electron microscopy (HRTEM) image (Fig. 4b) exhibits a representative structural detail of the enlarged region between the Ag and Au crystals. The individual lattice planes are clearly visible in the
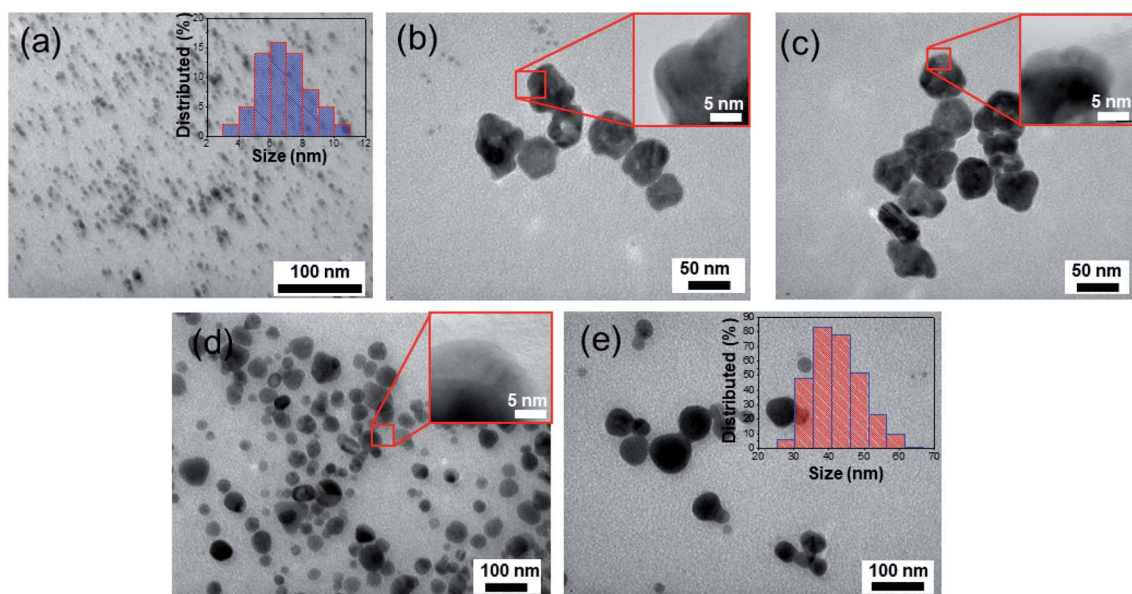

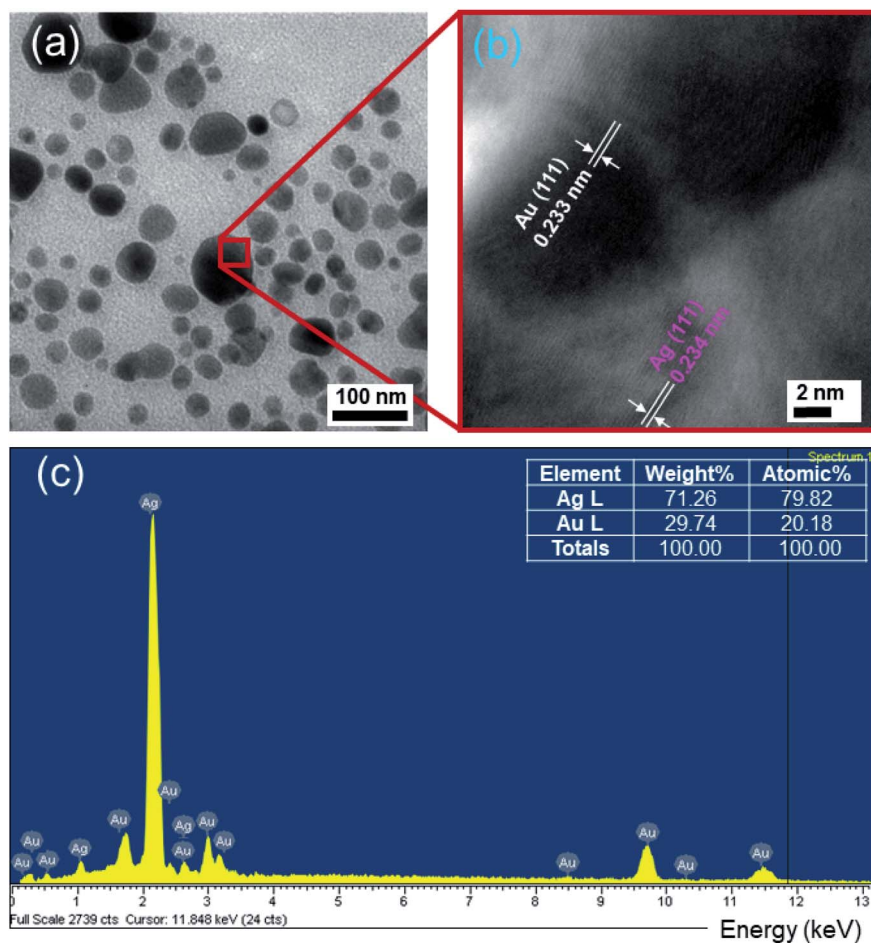**Fig. 3** TEM images of (a) Ag, (b) Ag$_3$Au, (c) AgAu, (d) AgAu$_3$, and (e) Au NPs.

Fig. 4 (a) TEM, (b) HRTEM images, and (c) EDS spectrum of the Ag_3Au NPs.

HRTEM picture. Evidently, it can be observed that the Ag crystals are indeed accreted together with Au crystals instead of a physical mixture of two different nanomaterials, owing to the obvious interconnected structure formed between the two crystals. The estimated interplanar spacing values of 0.234 nm for Ag and 0.233 nm for Au can be indexed as (111) in the face-centered cubic (FCC) crystal structure. The HRTEM image also revealed the single crystalline nature of the fabricated Ag/Au alloy NPs with a uniform atomic content. The lattice constants of Ag and Au are calculated according to the equation:[53]

$$d_{hkl}^2 = \frac{a^2}{h^2 + k^2 + l^2} \tag{5}$$

The obtained results are $a_{Ag} = 0.405$ nm, $a_{Au} = 0.403$ nm, in agreement with the literature values.[1] The quality of the synthesized NPs could be ascertained from the energy dispersive X-ray spectral (EDS) analysis, which reveals the elemental composition of the samples. The EDS spectrum in Fig. 4c unveils the presence of characteristic peaks for Ag, Au. Signals at 1 and 2.2 keV correspond to Ag. Less intense signals at 1.8, 3 and 9.8 keV are related to Au. The relative proportion of Ag to Au

in the alloy is 79.82 : 20.18, which is about 4 : 1 based on the EDS result. Variation in the intensity of signals from Au and Ag is observed to depend on the molar ratio of the respective elements in each of these samples. No impurity peaks were observed, confirming the high purity of the samples. The lattice constant of the Ag/Au alloy can be estimated following Vegard's law:[47]

$$a_{alloy} = na_{Ag} + ma_{Au} \tag{6}$$

where n and m are the atomic percentages of Ag and Au in the alloy. For the Ag_3Au alloy sample, $n = 0.7982$ and $m = 0.2018$, which are determined from the EDS spectrum in Fig. 4c. The calculated result is $a_{alloy} = 0.40495$ nm. The crystal structure of the samples is identical, but the lattice parameters have different values.

Because Ag and Au have the same face-centered cubic (FCC) crystal structure and very similar lattice constants, it is expected that no lattice mismatch is introduced by the incorporation of gold atoms because the difference in lattice constants is smaller than the amplitude of the thermal vibration of the atoms.[3] The absence of a boundary separating Ag and Au within the volume of the particle confirms the formation of the Ag/Au alloy.

3.3. Structural studies

The XRD analysis provided information about the crystalline structures of the Ag, Au and Ag₃Au alloy NPs. In Fig. 5a, the XRD pattern shows the intense and sharp peaks, which indicates the formation of NPs. Distinct diffraction peaks at scan angles 2θ of 38.18°, 44.38°, 64.57°, and 77.56°, indexing the (111), (200), (220) and (311) facets, respectively, of the face-centered cubic (FCC) crystalline structure, correlated with the Ag-ICDD card no. 01-071-3752. As seen in Fig. 5a, the high symmetry in the XRD peaks highlights the stable crystal structure with cubic geometry in the Ag₃Au sample.

The diffraction peaks from Ag/Au (JCPDS file no. 03-065-8424) can be observed. The XRD peaks at 2θ values of 38.27°, 44.49°, 64.73°, and 77.76° were matched with the (111), (200), (220), and (311) planes of the Ag/Au metal, respectively. By using the XRD patterns, it is possible to estimate the average crystalline sizes of the Ag, Au, Ag₃Au alloy *via* Debye–Scherrer formula by the measurement of the full width at half maximum (FWHM) of the (111) peak (Fig. 5b–d), and is found to be 28.36 nm, 8.14 nm and 7.3 nm, respectively, as reported:[4]

$$D = \frac{k\lambda}{\beta \cos \theta} \qquad (7)$$

where D is the average crystalline size in nanometers, λ is the wavelength of the used X-ray beam (0.154056 nm), k is the Scherrer constant (0.893), θ is the Bragg angle and β is the full width half maximum (FWHM) of the diffraction. Among samples, the smallest average crystallite size was determined for the Ag₃Au alloy at 7.3 nm and largest for the Ag sample at 28.36 nm. Because Au atoms have larger atomic sizes than Ag atoms, this affects the dimension of the crystals.

The functional groups of PVP involved in the reduction of metal ions and the formation of NPs were investigated by FTIR

spectroscopy. FTIR analyses of pure PVP and as-synthesized Ag/Au alloy NPs are shown in Fig. 6. The intense and distinct adsorption bands at 1652 cm⁻¹ and 3420 cm⁻¹ correspond to the carbonyl group (C=O) stretching vibration of pure PVP and the C–C stretching vibration, respectively. On the formation of the Ag/Au alloy NPs, the peaks shifted to 1641 and 2959 cm⁻¹, respectively. A visible shift in the band at 3420 cm⁻¹ to 2959 cm⁻¹ due to the O–H deformation in the FTIR spectrum of PVP.

The corresponding EDX elemental mapping images depicted in Fig. 7 show an overlapped distribution of Au and Ag atoms in the AgAu₃ sample. This result confirms the presence of Ag and Au atoms on the NPs, which is consistent with the alloy mode. It also indicated that the distribution of Ag and Au in the structure was homogeneous. In a word, we had successfully prepared uniform Ag/Au alloy nanoparticles.

3.4. SERS activity

Based on the above discussions, the obtained Ag/Au alloy NPs are expected to provide improved SERS activity in comparison with Ag or Au nanomaterials. Ag/Au bimetallic nanoparticles have been extensively applied in SERS studies.[43,44,52] As a demonstration of a practical application of the Ag/Au alloy NPs, we tested them as a SERS substrate to detect a standard model molecule. In this SERS experiment, rhodamine B (RhB) was selected as the probe molecule to examine the enhancement capability of various samples. A series of RhB solutions with concentrations from 10⁻⁵ to 10⁻¹¹ M have been prepared in advance through diluting proportionally by distilled water. The SERS analyses of RhB molecules adsorbed on the Ag/Au alloy NPs and AgNPs, AuNPs were performed using green
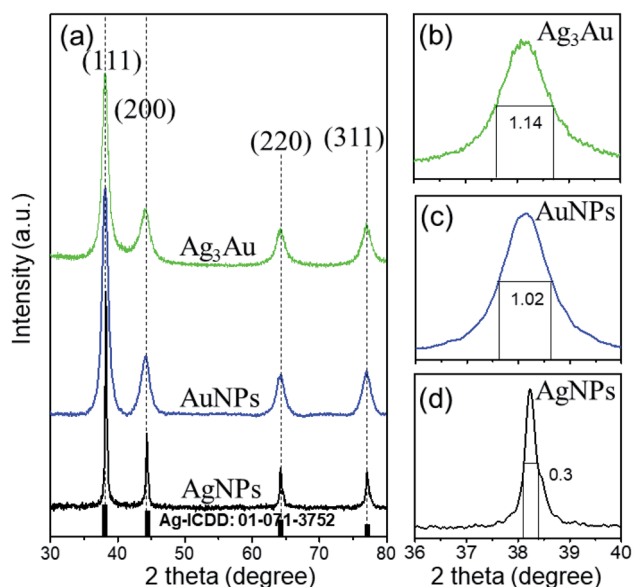

Fig. 5 (a) XRD of Ag, Au and Ag₃Au alloy NPs. FWHM of the (111) peak from (b) Ag₃Au, (c) Au, (d) Ag. The typical (111) reflection has the highest intensity.
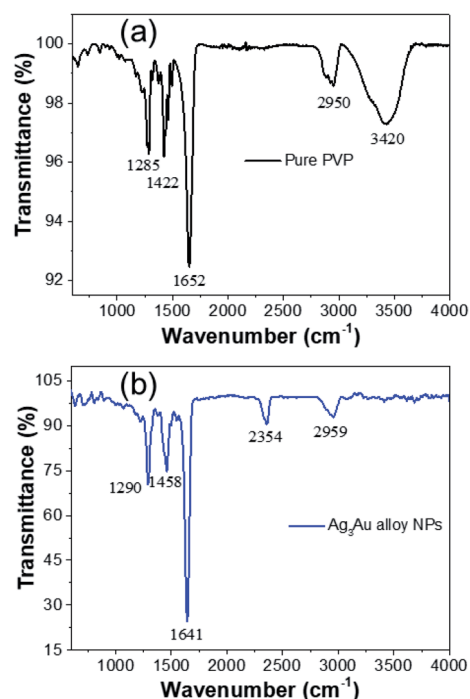

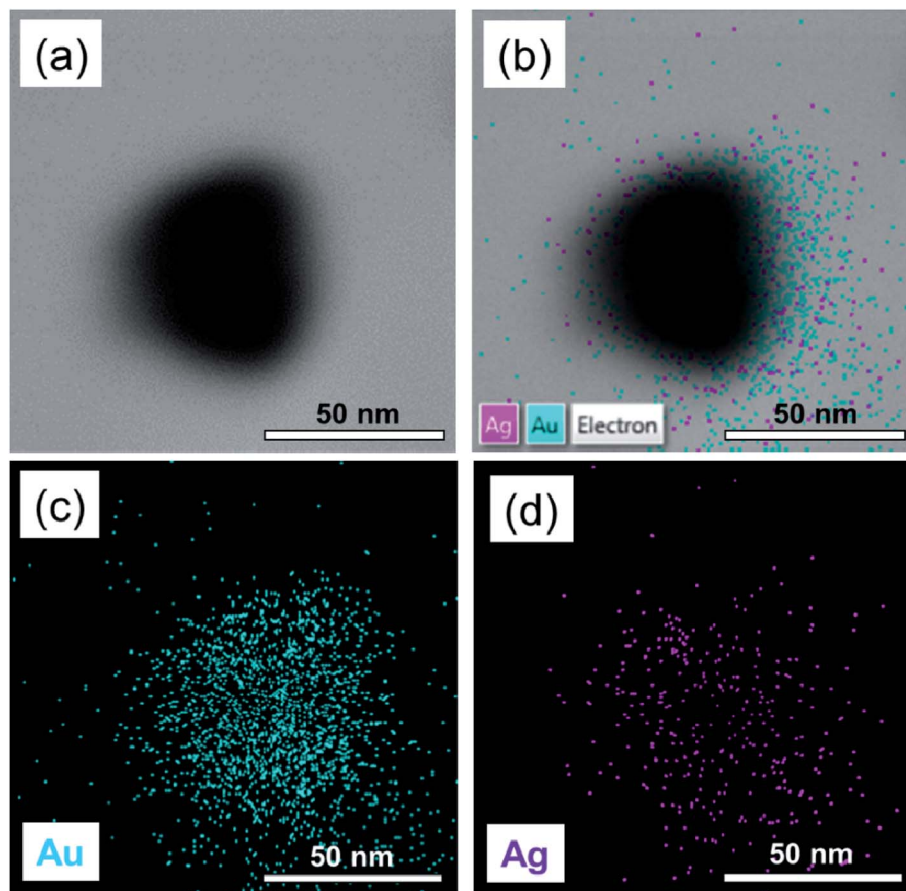**Fig. 6** FTIR spectra of the pure PVP (a) and Ag/Au alloy NPs (b).

Fig. 7   (a) TEM image of a single Ag–Au alloy nanoparticle and EDX elemental mapping images of the (b) overlay of Au and Ag, (c) Au, and (d) Ag.

532 nm laser excitation. After the substrate was dried completely, SERS measurements were performed. Fig. 8a shows the representative Raman spectrum of RhB (10^{-5} M) with prominent features between 1200 and 1650 cm^{-1}, which are regarded as the characteristic Raman peaks of RhB molecules. There was a significant peak in the SERS spectrum at a Raman shift 1650 cm^{-1} that was assigned to the stretching mode of the C=C bond. The other weak peaks at Raman shifts of around 1200, 1281, 1358, 1507 and 1528 cm^{-1} should belong to the xanthene ring puckering mode, stretching mode of the C–C bridge, bending mode of C–H, bending mode of C–C aromatic ring and bending mode of the C–H aromatic ring, respectively.[54] First, the AgNPs, AuNPs, and Ag/Au alloy NPs were dropped on silicon wafers to make SERS substrates. We found that the Raman signal scattered from the NPs without RhB is very weak and does not interfere with the SERS spectrum of the probe molecule (not shown here). In the case of RhB adsorbed on Ag/Au NPs, the Raman bands of the target molecules with molecular fingerprint were greatly enhanced in comparison with Ag or Au NPs, and allowed for easy detection of the analyte. Fig. 8b shows the SERS spectra collected from the same concentration of RhB solution (10^{-5} M) adsorbed on different SERS substrates (Ag, Au, Ag/Au alloy NPs with three Ag : Au ratios). It can be observed that the SERS spectra exhibited well-defined and high-resolution Raman spectral lines in the absence of any

background fluorescence. It is noted that the SERS intensity of the samples was related to the Ag : Au ratio; thus, we have to explore the enhanced capability of the nanoparticles with an optimal ratio. Furthermore, the intensity of the Raman signal increased gradually and then decreased as the Ag content increased, which reached the maximum at the Ag : Au molar ratio of 3 : 1 (Fig. 8c). Strongest SERS signals in the case of Ag_3Au could be attributed to the most hotspots generated in the Ag_3Au sample, which play a vital role in the enhancement of SERS.[55] Hence, from the view point of efficiency, the Ag_3Au alloy NPs could be considered as the optimal SERS substrate in detecting RhB. It is well known that the intensity of the SERS signal is affected by the plasmonic coupling of the metal interparticle. Additionally, the small size of NPs can cause their bigger surface and higher activity. The improved SERS activity originates from a pronounced electromagnetic field under optical resonant condition between LSPR of the SERS substrate and the incident laser wavelength.[52] Besides the EM enhancement, the chemical enhancement derived from the charge-transfer between the probe molecules and substrate provides a contribution for improving the SERS activity. The chemical (CM) enhancement originates from the charge-transfer (CT) mechanism between the metal and probe RhB molecules. Ag or Au NPs can be efficiently excited by green 532 nm laser excitation, resulting in an enhanced CT effect for improving the SERS
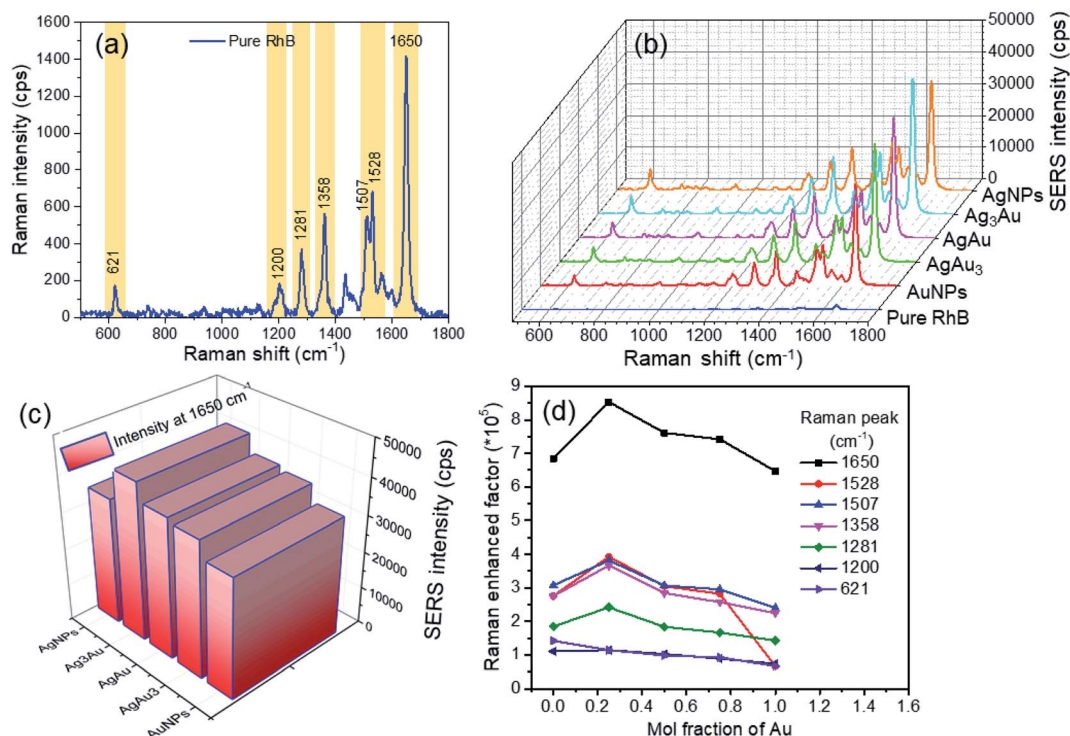
Fig. 8 SERS spectra of RhB (10^{-5} M) acquired from different substrates: (a) pure RhB (blank silicon wafer), (b) pure Ag, pure Au, Ag/Au alloy NPs, (c) SERS intensity of the 1650 cm^{-1} peak, (d) EF values as a function of concentration.

intensity. The electronic interaction between the Ag/Au NPs and SiO$_2$ gives rise to the formation of an internal electric field, providing additional CM contribution for increasing the SERS signal.

The SERS enhancement factor of our Ag/Au alloy NPs was calculated by comparing the acquired signals from the substrate with and without AgNPs, AuNPs, or Ag/Au alloy NPs. In the present study, the analytical SERS enhancement factor (EF) of RhB molecules adsorbed on the obtained Ag, Au or Ag/Au alloy NPs can be estimated according to the expression:

$$\text{EF} = \frac{I_{\text{SERS}}}{I_{\text{nor}}} \times \frac{C_{\text{nor}}}{C_{\text{SERS}}} \qquad (8)$$

where I_{SERS} is the SERS signal intensity of RhB adsorbed on the metallic nanostructure substrate, I_{nor} indicates the signal intensity of a normal Raman spectrum of the same vibration peak for the RhB molecule on the silicon wafer (without NPs), C_{SERS} represents the RhB concentration on substrates exposed

to the laser spot focused area and $C_{\text{nor}} = 10^{-4}$ M is the RhB concentration in a normal Raman spectrum, which produces the Raman signal (I_{nor}) acquired at the same conditions. There are 7 spectral features at 621, 1200, 1281, 1358, 1507, 1528 and 1650 cm^{-1}, which can be used for directly quantitatively determining the EF values of various Ag/Au proportions for 10^{-5} M RhB (Table 1). According to the spectra shown, the peak around 1650 cm^{-1} was the most representative one; its intensity was very sensitive to the RhB concentration and its EF has the highest values compared with other peaks. Therefore, it was chosen as an ideal peak for the quantitative analysis of RhB and to calculate the EF values. The lowest EF was observed for the pure AgNPs and pure AuNPs because the NP aggregation is the lowest. The Ag substrate depicting the SERS EF for the band at 1650 cm^{-1} was calculated to be $\sim$6.8 $\times$ 10^5, which is slightly higher than the result reported for the Au substrate ($\sim$6.4 $\times$ 10^5). The largest Raman activity achieved at the Ag$_3$Au alloy NP-based substrate with an analytical enhancement factor of 8.5 $\times$

Table 1 EF values calculated from the characteristic peaks for 10^{-5} M RhB

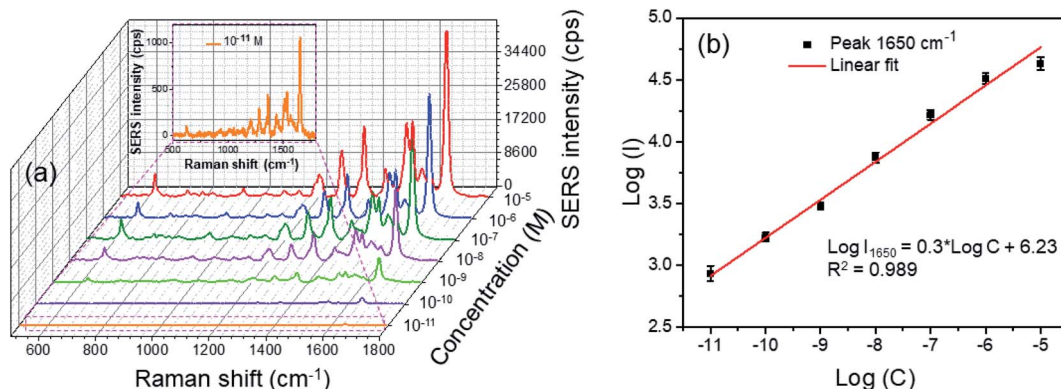| Substrate used	1650 cm^{-1}	1528 cm^{-1}	1507 cm^{-1}	1358 cm^{-1}	1281 cm^{-1}	1200 cm^{-1}	621 cm^{-1}
Au	6.4×10^5	6.5×10^5	2.4×10^5	2.2×10^5	1.4×10^5	7.3×10^4	6.61×10^4
AgAu$_3$	7.4×10^5	2.8×10^5	2.9×10^5	2.5×10^5	1.6×10^5	8.8×10^4	9.21×10^4
AgAu	7.6×10^5	3.0×10^5	3.0×10^5	2.8×10^5	1.8×10^5	1.0×10^5	9.81×10^4
Ag$_3$Au	8.5×10^5	3.9×10^5	3.8×10^5	3.6×10^5	2.4×10^5	1.0×10^5	1.11×10^5
Ag	6.8×10^5	2.7×10^5	3.0×10^5	2.7×10^5	1.8×10^5	1.0×10^5	1.41×10^5

Fig. 9 (a) SERS spectra from the Ag$_3$Au alloy NP-based substrate with various concentrations of RhB from 10^{-11} to 10^{-5} M. (b) The plot of the concentration vs. 1650 cm^{-1} peak intensity in logarithm scale. The data points seem to fit a linear dependence (solid line). The error bars correspond to twice the experimental standard deviation.

10^5 was higher than the counterparts made of Ag or Au. The aggregation effect between silver and gold induces a much shorter distance between the dye molecules and NPs, and provides high-density homo-hotspots (Ag–Ag) and hetero-hotspots (Ag–Au), which endow these alloy NPs with extraordinary SERS enhancement ability.[31] Additionally, from Table 1, we found that the EF value for Ag is higher than that for Au, which agreed with the basic theory of SERS.[56] The EF values were calculated for all SERS peaks and plotted as a function of Ag content, which is presented in Fig. 8d. The decrease in EF to ~7.4 × 10^5 when the Au content increased from 50% to 75% might be because of the over-aggregation of NPs. The excess Au may possibly inhibit the formation of hotspots, so the number of SERS-active hotspots is limited. Therefore, these samples achieved inferior SERS signal. As the spectral position of the bands in the SERS measurements are nearly unchanged, the EM enhancement is reasonably responsible for the high SERS signal intensity.

Fig. 9a shows the RhB concentration-dependent SERS spectra of the Ag$_3$Au alloy NPs in aqueous solution in the range of 10^{-11} to 10^{-5} M. The signal is very tiny when the amount of RhB is relatively small. With increasing concentration of the dye solution, the number of molecules adsorbed on the substrate increased and the Raman signal intensity became stronger. The high concentration of RhB shows more energetic SERS activity. The strongest peak at a Raman shift of 1650 cm^{-1} was chosen as the characteristic peak of RhB. For the 10^{-5} M RhB solution, the signal intensity was very strong (about 35 000 a.u.). Even at a RhB concentration down to 10^{-11} M, the fairly strong SERS signal intensity was still distinguishable (about 1000 a.u., inset of Fig. 9a), which was indicative of the excellent enhancement of our substrate. The estimated EF values calculated at the 1650 cm^{-1} peak from different concentrations of RhB are indicated in Table 2. The EF value can reach up to 2 × 10^{10}

toward the RhB concentration of 10^{-11} M. Characteristic signals illustrate that the low SERS limit of detection (LOD) can be achieved at the picomole level (~10 pM). This is because the dominating characteristic band of the RhB molecules was clear even when the concentration decreased to as low as 10^{-11} M, much lower than the reported value (5 × 10^{-9} M) obtained from core–shell Au@Ag nanoparticles.[33] To our best knowledge, the minimum detection limit was 10^{-12} M in the ref. 57, so the Ag/Au alloy NPs could donate the equivalent SERS detection limit. This indicated that the prepared Ag/Ag alloy NPs have great potential of application as a standard tool for the detection of food contamination, as well as many SERS-related fields.

On the other hand, the relationship between the logarithm of the SERS intensity of peak 1650 cm^{-1} and logarithm of the RhB concentration is plotted in Fig. 9b, where the y-axis corresponds to the Raman peak intensity at 1650 cm^{-1} and the x-axis corresponds to the RhB concentration (in log scale). This showed a monotonic increase of the Raman intensity with RhB concentration. The linear calibration curve was constructed by monitoring the logarithm of the intensity of the strong 1650 cm^{-1} spectral feature as a function of the analyte concentration. The fitted curve could be mathematically expressed as follows:

$$\log I = 0.3 \log C + 6.23 \qquad (9)$$

where I was the SERS intensity of the 1650 cm^{-1} peak, and C was the RhB concentration in a wide range of 10^{-11} to 10^{-5} M. The correlation coefficient (R^2) of 0.989 was an approximately linear relation.

The SERS enhancement mainly resulted from the strong local electromagnetic field induced by LSPR.[58] The SERS enhancement factor (EF) should be proportional to:

Table 2 EF values calculated at the 1650 cm^{-1} peak from different concentrations of RhB using Ag$_3$Au NPs as a substrate

RhB (M)	10^{-5}	10^{-6}	10^{-7}	10^{-8}	10^{-9}	10^{-10}	10^{-11}
EF value	8.5 × 10^5	6.4 × 10^6	3.3 × 10^7	4.4 × 10^7	8 × 10^8	3 × 10^9	2 × 10^{10}

$$\text{EF} \sim \left(\frac{a}{a+d}\right)^{12} \tag{10}$$

where a is the radius of the Ag/Au NP ($a \sim 40$–60 nm), and d is the distance between the center of the adsorbate groups and the surface of the particle.[31] The SERS signal is considerably enhanced when NPs are aggregated through the hotspots created between neighboring metal particles. The plasmon coupling at the hotspots can provide a high local EM field, which is expected to contribute to the distance-dependent SERS enhancement.

The homogeneity of the SERS signal is a significant parameter in evaluating the practicality of the SERS substrates.[2] As shown in Fig. 10, in order to further prove the reproducibility of the Ag$_3$Au NP-based SERS substrate, 8 Raman spectra were acquired at randomly selected sites on the substrate, and the analyzing concentration of RhB was 10^{-11} M. The histogram of the SERS intensity in Fig. 10a shown no significant variations in the EF, and the observed EF was $\sim 2 \times 10^{10}$. The relative standard deviation (RSD) value calculated from the SERS signal intensity at the prominent peak of 1650 cm^{-1} from different spots was 3.1% (Fig. 10b), revealing reproducible and accurate data. The high spot-to-spot reproducibility may result from the uniformity of the hotspots. When a solution was dropped on a substrate, the nanoparticles in the solution were favorably deposited in the edge region at higher concentration than in the central region, which is called the coffee ring effect.[30] However, the tiny shape droplets could be very effective and convenient to generate a uniform distribution of the Ag/Au NPs/RhB mixture

on the substrate. From the observed results, it can be concluded that the Ag$_3$Au NPs sample demonstrated a highly sensitive and reproducible SERS response with relatively low RSD value. On the other hand, Fig. 10c exhibits the SERS spectra of RhB molecules adsorbed on the Ag$_3$Au alloy NPs substrates before and after storage for 1 year at room temperature. The Raman signal intensity of the 1650 cm^{-1} peak slightly decreased from about 1600 a.u. for an as-prepared substrate to 1300 a.u. after 1 year, supporting that nearly 80% SERS intensity can be maintained during this storage. It reveals that no significant change can be observed in both the peak position and the intensity. It is concluded that the Au content in the Ag/Au alloy can significantly improve the stability of the SERS substrates. The results are in agreement with the previous reports.[34,38] Although the long exposure time to the air will result in the loss of SERS activity, all of these experimental results in this paper confirm that the Ag/Au alloy NPs overcome the limitation of the oxidation of AgNPs and serve as efficient and stable SERS-based RhB sensing using the 532 nm wavelength laser as an excitation source. This advantage shows more potential in developing a more effective spectroscopic sensor in detecting the RhB dye.

4. Conclusions

In summary, we have shown that the Ag/Au alloy NPs with various compositions and sizes can be synthesized by a simple co-reduction method. This process was effective, productive and the proportion of Ag to Au in the alloy NPs was adjustable by controlling the Ag$^+$: Au^{3+} molar ratio in the salt mixture
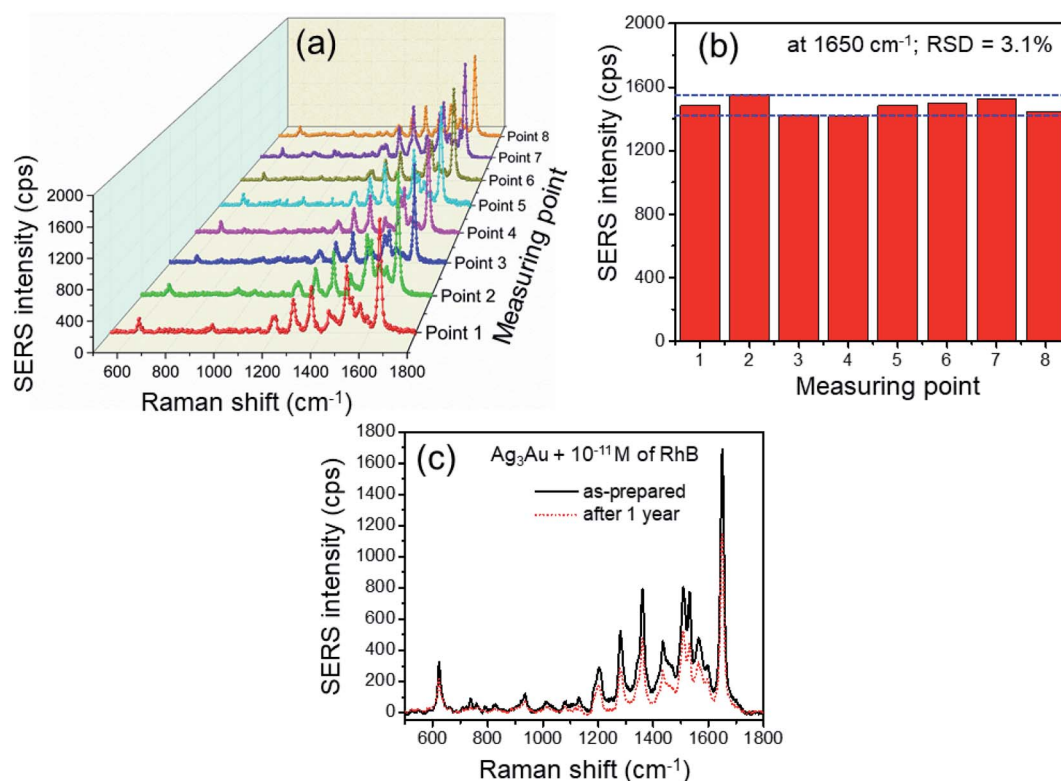

Fig. 10 (a) SERS spectra of RhB from different spots of the Ag$_3$Au substrate. (b) Histogram of the peak intensity at 1650 cm^{-1} with a RSD of 3.1%. (c) SERS spectra of 10^{-11} M RhB molecules before and after storage for 1 year at room temperature.

solution. The absorption peak of the Ag/Au alloy red-shifted when decreasing the molar ratio of $Ag^+ : Au^{3+}$, corresponding with the change of the particle size. Thus, the co-reduction provided a suitable and flexible way for producing different compositions and size-controlled Ag/Au alloy NPs. The drop-coated Ag/Au alloy NPs film was ordered and uniform, which was well adapted for the SERS substrate with good reproducibility and high SERS activity. The NPs were loaded on a silicon wafer for an optimally aggregated configuration to yield the maximum signal enhancement in the SERS measurements. The Ag_3Au NPs exhibited the optimal SERS performance for the 532 nm excitation. The optimized active SERS substrate is helpful for the detection of RhB molecules with high sensitivity. The SERS measurements for the RhB solution showed that the Ag/Au alloy NPs exhibited strong SERS performance, and the detection limit can reach as low as 10^{-11} M with EF over 10^{10}. We can achieve good reproducibility with the RSD value below 4% at different locations. Owing to the attractive features, such as feasible fabrication method and easy-to-perform detection, the Ag_3Ag alloy NPs will be a prospective candidate for SERS application in environmental monitoring, food safety analysis and the rapid detection of RhB.

Conflicts of interest

The authors declare that they have no competing interests. The authors alone are responsible for the content and writing of the paper. All authors read and approved the final manuscript.

Acknowledgements

References

1 V. C. Long, V. D. Quoc and D. N. Trong, *ACS Omega*, 2020, **5**, 31391–31397.

2 S. S. B. Moram, C. Byram, S. N. Shibu, B. M. Chilukamarri and V. R. Soma, *ACS Omega*, 2018, **3**, 8190–8201.

3 S. Link, Z. L. Wang and M. A. El-Sayed, *J. Phys. Chem. B*, 1999, **103**, 3529–3533.

4 O. M. Ozkendir, E. Cengiz, E. Yalaz, O. Sogut, D. H. Ayas and B. N. Thammajak, *J. Electron Spectrosc. Relat. Phenom.*, 2016, **209**, 53–61.

5 L. Feng, G. Gao, P. Huang, K. Wang, X. Wang, T. Luo and C. Zhang, *Nano Biomed. Eng.*, 2010, **2**, 258–267.

6 J. R. G. Navarro and M. H. V. Werts, *Analyst*, 2013, **138**, 583–592.

7 K. Yuan, J. Zheng, D. Yang, B. J. Sanchez, X. Liu, X. Guo, C. Liu, N. E. Dina, J. Jian, Z. Bao, Z. Hu, Z. Liang, H. Zhou and Z. Jiang, *ACS Omega*, 2018, **3**, 2855–2864.

8 V. Vilas, D. Philip and J. Mathew, *J. Mol. Liq.*, 2016, **221**, 179–189.

9 H. T. Nasrabadi, E. Abbasi, S. Davaran, M. Kouhi and A. Akbarzadeh, *Artif. Cells, Nanomed., Biotechnol.*, 2016, **44**, 376–380.

10 A. Loiseau, V. Asila, G. Boitel-Aullen, M. Lam, M. Salmain and S. Boujday, *Biosensors*, 2019, **9**, 1–39.

11 L. Xu, Z. Luo, Z. Fan, X. Zhang, C. Tan, H. Li, H. Zhang and C. Xue, *Nanoscale*, 2014, **6**, 11738–11743.

12 N. G. Bastus, F. Merkoci, J. Piella and V. Puntes, *Chem. Mater.*, 2014, **26**, 2836–2846.

13 R. Deng, H. Qu, L. Liang, J. Zhang, B. Zhang, D. Huang, S. Xu, C. Liang and W. Xu, *Anal. Chem.*, 2017, **89**, 2844–2851.

14 K. S. Abhijith, R. Sharma, R. Ranjan and M. S. Thakur, *Photochem. Photobiol. Sci.*, 2014, **13**, 986–991.

15 V. Bastys, I. Pastoriza-Santos, B. Rodriguez-Gonzalez, R. Vaisnoras and L. M. Liz-Marzan, *Adv. Funct. Mater.*, 2006, **16**, 766–773.

16 Y. Yang, Q. Zhang, Z.-W. Fu and D. Qin, *ACS Appl. Mater. Interfaces*, 2014, **6**, 3750–3757.

17 A. V. Girao, P. C. Pinheiro, M. Ferro and T. Trindade, *RSC Adv.*, 2017, **7**, 15944–15951.

18 A. Childs, E. Vinogradova, F. Ruiz-Zepeda, J. J. Velazquez-Salazar and M. Jose-Yacaman, *J. Raman Spectrosc.*, 2016, **47**, 651–655.

19 J. Piella, N. G. Bastus and V. Puntes, *Chem. Mater.*, 2016, **28**, 1066–1075.

20 C. Wang, S. Peng, R. Chan and S. Sun, *Small*, 2009, **5**, 567–570.

21 V. D. Chinh and N. Q. Trung, *Int. J. Nanotechnol.*, 2015, **12**, 515–523.

22 L. Sun, W. Luan and Y. J. Shan, *Nanoscale Res. Lett.*, 2012, **7**, 1–6.

23 J. Li, B. Tian, T. Li, S. Dai, Y. Weng, J. Lu, X. Xu, Y. Jin, R. Pang and Y. Hua, *Int. J. Nanomed.*, 2018, **13**, 1411–1424.

24 B. Nie, Y. Luo, J. Shi, L. Gao and G. Duan, *Sens. Actuators, B*, 2019, **301**, 1–9.

25 V. Turzhitsky, L. Zhang, G. L. Horowitz, E. Vitkin, U. Khan, Y. Zakharov, L. Qiu, I. Itzkan and L. T. Perelman, *Small*, 2018, **14**, 1–11.

26 W. Zhang, B. Li, L. Chen, Y. Wang, D. Gao, X. Ma and A. Wu, *Anal. Methods*, 2014, **6**, 2066–2071.

27 Y. Zhao, Y.-J. Zhang, J.-H. Meng, S. Chen, R. Panneerselvam, C.-Y. Li, S. B. Jamali, X. Li, Z.-L. Yang, J.-F. Li and Z.-Q. Tian, *J. Raman Spectrosc.*, 2016, **47**, 662–667.

28 M. Fleischmann, P. J. Hendra and A. J. McQuillan, *Chem. Phys. Lett.*, 1974, **26**, 163–166.

29 S. Nie and S. R. Emony, *Science*, 1997, **275**, 1102–1106.

30 B. Li, W. Zhang, L. Chen and B. Lin, *Electrophoresis*, 2013, **34**, 2162–2168.

31 E.-O. Ganbold, J.-H. Park, U. Dembereldorj, K.-S. Ock and S.-W. Joo, *J. Raman Spectrosc.*, 2011, **42**, 1614–1619.

32 H. Chen, S.-G. Park, N. Choi, J.-I. Moon, H. Dang, A. Das, S. Lee, D.-G. Kim, L. Chen and J. Choo, *Biosens. Bioelectron.*, 2020, **167**, 1–8.

33 H. Wang, X. Guo, S. Fu, T. Yang, Y. Wen and H. Yang, *Food Chem.*, 2015, **188**, 137–142.

34 D. Xu, H. Jiang, S. Zhang, W. Yang, Y. Zhang, Z. Wang and J. Chen, *Microchem. J.*, 2020, **158**, 1–6.

35 R. Mei, Y. Wang, Q. Yu, Y. Yin, R. Zhao and L. Chen, *ACS Appl. Mater. Interfaces*, 2020, **12**, 2059–2066.

36 J.-J. Li, C. Wu, J. Zhao, G.-J. Weng, J. Zhu and J.-W. Zhao, *Spectrochim. Acta, Part A*, 2018, **204**, 380–387.

37 H. S. S. Sharma, E. Carmichael and D. McCall, *Vib. Spectrosc.*, 2016, **83**, 159–169.

38 B. Mir-Simon, J. Morla-Folch, P. Gisbert-Quilis, N. Pazos-Perez, H.-n. Xie, N. G. Bastus, V. Puntes, R. A. Alvarez-Puebla and L. Guerrini, *J. Opt.*, 2015, **17**, 1–9.

39 S. Das, B. Satpati, T. S. Bhattacharya and T. Bala, *Nano-Struct. Nano-Objects*, 2020, **22**, 100438.

40 L. ur-Rahman, A. Shah, S. B. Khan, A. M. Asiri, H. Hussain, C. Han, R. Qureshi, M. N. Ashiq, M. A. Zia, M. Ishaq and H.-B. Kraatz, *J. Appl. Electrochem.*, 2015, **45**, 463–472.

41 X. Su, Y. Wang, W. Wang, K. Sun and L. Chen, *ACS Appl. Mater. Interfaces*, 2016, **8**, 10201–10211.

42 H. J. Yin, Z. Y. Chen, Y. M. Zhao, M. Y. Lv, C. A. Shi, Z. L. Wu, X. Zhang, L. Liu, M. L. Wang and H. J. Xu, *Sci. Rep.*, 2015, **5**, 1–9.

43 Y. Yang, J. Liu, Z.-W. Fu and D. Qin, *J. Am. Chem. Soc.*, 2014, **136**, 8153–8156.

44 Y. Ran, P. Strobbia, V. Cupil-Garcia and T. Vo-Dinh, *Sens. Actuators, B*, 2019, **287**, 95–101.

45 X. Jiang, Z. Tan, L. Lin, J. He, C. He, B. D. Thackray, Y. Zhang and J. Ye, *Small Methods*, 2018, **1800182**1–14.

46 G. Frens, *Nat. Phys. Sci.*, 1973, **241**, 20–22.

47 T. T. H. Pham, X. H. Vu, N. D. Dien, T. T. Trang, N. V. Truong, T. D. Thanh, P. M. Tan and N. X. Ca, *RSC Adv.*, 2020, **10**, 24577–24594.

48 N. G. Bastus, J. Comenge and V. Puntes, *Langmuir*, 2011, **27**, 11098–11105.

49 P. Mulvaney, *Langmuir*, 1996, **12**, 788–800.

50 S. W. Verbruggen, M. Keulemans, J. A. Martens and S. Lenaerts, *J. Phys. Chem. C*, 2013, **117**, 19142–19145.

51 H. Zhang, L. Xu, Y. Tian, M. Chen, X. Liu and F. Chen, *Opt. Express*, 2017, **25**, 29389–29400.

52 A. Jiao, H. Zhang, L. Xu, Y. Tian, X. Liu, M. Chen and F. Chen, *Opt. Express*, 2019, **27**, 23981–23995.

53 H. Mao, J. Feng, X. Ma, C. Wu and X. Zhao, *J. Nanopart. Res.*, 2012, **14**, 1–15.

54 N. T.-Q. Luong, D. T. Cao, C. T. Anh, K. N. Minh, N. N. Hai and L. V. Vu, *J. Electron. Mater.*, 2019, **48**, 5328–5332.

55 M. J. Ashley, M. R. Bourgeois, R. R. Murthy, C. R. Laramy, M. B. Ross, R. R. Naik, G. C. Schatz and C. A. Mirkin, *J. Phys. Chem. C*, 2018, **122**, 2307–2314.

56 V. K. Rao and T. P. Radhakrishnan, *ACS Appl. Mater. Interfaces*, 2015, **7**, 12767–12773.

57 C. Fang, A. Agarwal, K. D. Buddharaju, N. M. Khalid, S. M. Salim, E. Widjaja, M. V. Garland, N. Balasubramanian and D.-L. Kwong, *Biosens. Bioelectron.*, 2008, **24**, 216–221.

58 J. D. Weatherston, N. C. Worstell and H.-J. Wu, *Analyst*, 2016, **141**, 6051–6060.